

# Comprehensive Study of Pyrido[3,4-*b*]pyrazine-Based D- $\pi$ -A Copolymer for Efficient Polymer Solar Cells

Yu-Qi Wu,<sup>1</sup> Hsieh-Chih Chen,<sup>2,3</sup> Yun-Siou Yang,<sup>1</sup> Sheng Hsiung Chang,<sup>2</sup>  
Pin-Jiun Wu,<sup>4</sup> Yen-Yi Chu,<sup>4</sup> Chun-Guey Wu<sup>1,2</sup>

<sup>1</sup>Department of Chemistry, National Central University, Taoyuan City 32001, Taiwan

<sup>2</sup>Research Center for New Generation Photovoltaics, National Central University, Taoyuan City 32001, Taiwan

<sup>3</sup>Graduate Institute of Energy Engineering, National Central University, Taoyuan City 32001, Taiwan

<sup>4</sup>National Synchrotron Radiation Research Center, Hsinchu 30076, Taiwan

Correspondence to: H.-C. Chen (E-mail: austinch@ncu.edu.tw) or C.-G. Wu (E-mail: t610002@cc.ncu.edu.tw)

Received 24 September 2015; accepted 5 January 2016; published online 29 January 2016

DOI: 10.1002/pola.28044

**ABSTRACT:** Two D- $\pi$ -A copolymers, based on the benzo[1,2-*b*:4,5-*b'*]-dithiophene (BDT) as a donor unit and benzoquinoxaline (BQ) or pyrido-quinoxaline (PQ) analog as an acceptor (PBBDT-TBQ and PBBDT-TPQ), were designed and synthesized as a p-type material for bulk heterojunction (BHJ) photovoltaic cells. When compared with the PBBDT-TBQ polymer, PBBDT-TPQ exhibits stronger intramolecular charge transfer, showing a broad absorption coverage at the red region and narrower optical bandgap of 1.69 eV with a relatively low-lying HOMO energy level at -5.24 eV. The experimental data show that the exciton dissociation efficiency of PBBDT-TPQ:PC<sub>71</sub>BM

blend is better than that in the PBBDT-TBQ:PC<sub>71</sub>BM blend, which can explain that the IPCE spectra of the PBBDT-TPQ-based solar cell were higher than that of the PBBDT-TBQ-based solar cell. The maximum efficiency of PBBDT-TPQ-based device reaches 4.40% which is much higher than 2.45% of PBBDT-TBQ, indicating that PQ unit is a promising electron-acceptor moiety for BHJ solar cells. © 2016 Wiley Periodicals, Inc. *J. Polym. Sci., Part A: Polym. Chem.* **2016**, *54*, 1822–1833

**KEYWORDS:** bulk heterojunction; quinoxaline; solar cells; structure-function relationship; time-resolved photoluminescence

**INTRODUCTION** Organic photovoltaics (OPVs) have recently become popular because of their advantages, including low cost, light weight, flexibility, and solution processability over conventional solar cells.<sup>1</sup> One of the most commonly used OPV device architectures is a bulk heterojunction (BHJ), which is composed of an active layer of a p-type polymer and an n-type fullerene blended together to form a bicontinuous interpenetrating network for efficient exciton diffusion, charge separation, and charge transport flanked by two electrodes.<sup>2,3</sup> It has been recognized that an ideal polymer donor in OPVs should represent broader absorption with high absorption coefficient in the visible and near-infrared region, high hole mobility, and suitable electronic energy levels matching the fullerene acceptor.<sup>2,3</sup> In this regard, the combination of alternating electron-rich donor (D) and electron-deficient acceptor (A) moieties along the backbone is a powerful strategy in designing narrow bandgap conjugated polymer with broad absorbance.<sup>4–14</sup> Thus, seeking novel efficient donor and acceptor units to develop well-performed

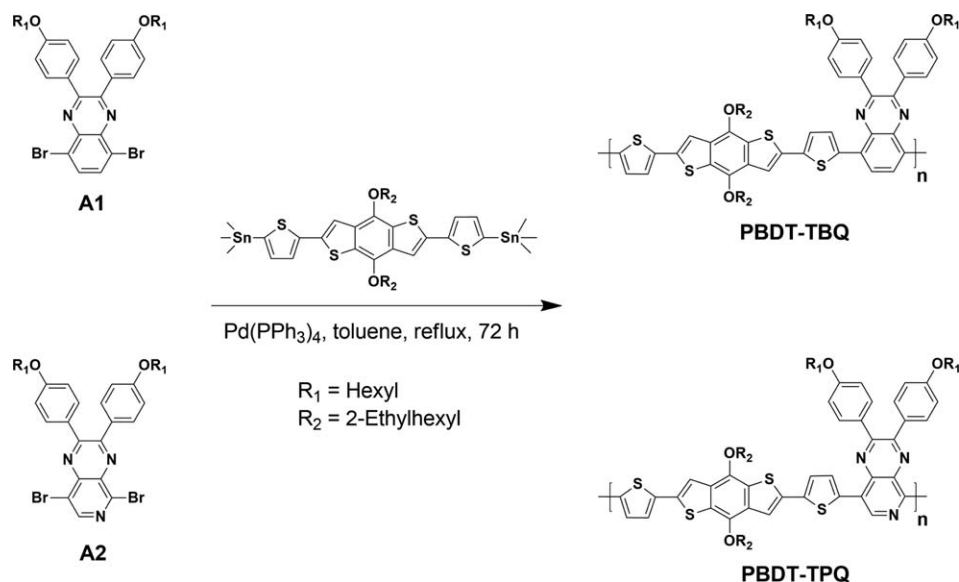
p-type conjugated polymers is of great significance in BHJ solar cells. Through prolonged effort, the record of power conversion efficiencies (PCEs) has been achieved in excess of 8–10% for single-junction solar cells.<sup>15–23</sup> Nowadays, a number of strategies have been developed to achieve the PCEs of 10–15% for commercialization on various principles, such as the design of novel material systems and the device architecture amelioration, with a view to enhance the light absorption and tuning of the energy band structure of the blended active layers.<sup>24–32</sup>

Benzo[1,2-*b*:4,5-*b'*]-dithiophene (BDT) is a representative donor block for high-mobility polymer semiconductors because of its rigidity, coplanarity by fusing a benzene with two flanking thiophene units, high hole mobility, extremely extended  $\pi$ -conjugation, favorable interchain  $\pi$ - $\pi$  stacking, and proper side chain patterns for enhanced solubility.<sup>33–35</sup> In addition, quinoxaline derivatives with two electron-withdrawing imine nitrogen atoms are of particular interest as electron-accepting moieties are not only easily modified but also side-substituted to finely

Y.-Q. Wu and H.-C. Chen contributed equally to this work.

Additional Supporting Information may be found in the online version of this article.

© 2016 Wiley Periodicals, Inc.



**SCHEME 1** Schematic illustration of the procedure for the preparation of PBTD-TBQ and PBTD-TPQ copolymers.

tune the optoelectronic properties of the resulting polymers.<sup>12–15</sup> Therefore, how to rationally design suitable substituents within quinoxaline derivatives in combination with BDT unit to achieve high photovoltaic performance p-type polymer is highly desirable and of particular importance.

In this context, we introduced a new strategy to modify quinoxaline moiety by incorporating pyridine substitution into the quinoxaline unit. Therefore, the replacement of substitution of the 6-position carbon with nitrogen could offer an additional opportunity to alternate the electronegativity of quinoxaline derivatives. Here, we report a straightforward synthetic methodology to prepare two medium bandgap conjugated D– $\pi$ –A copolymers composed of a BDT donor unit coupled with benzo-quinoxaline (BQ) or pyrido-quinoxaline (PQ) acceptor segments bridged by a thiophene (see Scheme 1). The preliminary results showed that PBTD-TPQ polymer could be a promising candidate for solar cell applications.

## EXPERIMENTAL

### Synthesis of Precursors and Polymers

#### Synthesis of 3,6-Dibromo-1,2-benzenediamine (**M1**)

4,7-Dibromo-2,1,3-benzothiadiazole (0.7 g, 2.4 mmol) in ethyl alcohol (80 mL) was cooled to 0 °C, and then under argon, sodium borohydride (2.0 g, 52.0 mmol) was added. After being stirred at 0 °C for 10 min, the reaction mixture was stirred at room temperature for another 20 h. After being cooled to 0 °C, the reaction mixture was treated with distilled water (20 mL) to quench the reaction. After removing the solvent under reduced pressure, the residue was diluted with ether and subsequently purified by column chromatography on silica gel using ethyl acetate/hexane (= 1/3) as an eluent to afford compound **M1** (0.56 g, 86%).

<sup>1</sup>H NMR (CDCl<sub>3</sub>, 300 MHz,  $\delta$ ): 6.84 (s, 2H), 3.89 (br, 4H). <sup>13</sup>C NMR (CDCl<sub>3</sub>, 300 MHz,  $\delta$ ): 109.41, 123.41, 133.86. HR-FAB MS *m/z* calcd for C<sub>6</sub>H<sub>6</sub>Br<sub>2</sub>N<sub>2</sub> [M<sup>+</sup>]: 265.9364; found: 265.8875.

#### Synthesis of 2,5-Dibromopyridine-3,4-diamine (**M2**)

Pyridine-3,4-diamine (5.0 g, 45.8 mmol) and 48% HBr<sub>(aq)</sub> (62 mL) were added into a 250-mL flask, followed by slowly adding Br<sub>2</sub> (7.5 mL) dropwise. The reaction mixture was refluxed for 12 h. After cooling, the raw product was collected by filtration and washed using saturated Na<sub>2</sub>S<sub>2</sub>O<sub>3</sub> aqueous solution, saturated NaHCO<sub>3</sub> aqueous solution, and deionized water successively. The crude product was purified by column chromatography on silica gel using ethyl acetate/hexane (= 1/2) as an eluent to afford compound **M2** (6.5 g, 53%).

<sup>1</sup>H NMR (CDCl<sub>3</sub>, 300 MHz,  $\delta$ ): 7.86 (s, 1H), 4.47 (br, 2H), 3.65 (br, 2H). <sup>13</sup>C NMR (CDCl<sub>3</sub>, 300 MHz,  $\delta$ ): 106.88, 128.41, 130.14, 141.22, 142.10. HR-FAB MS *m/z* calcd for C<sub>5</sub>H<sub>5</sub>Br<sub>2</sub>N<sub>3</sub> [M<sup>+</sup>]: 266.92; found: 266.8827.

#### Synthesis of 4,4'-Dihexyloxybenzil (**M3**)

A mixture of 4,4'-dihydroxybenzil (1.0 g, 4.1 mmol), 1-bromohexane (1.3 mL, 9.0 mmol), tetra-*n*-butylammonium bromide (1.2 g, 4.1 mol), and potassium carbonate (1.2 g, 8.2 mol) in DMF (10 mL) was stirred at 100–120 °C for 2 h. The reaction mixture was diluted with water, and the redundant precipitate was filtered and washed with water (3  $\times$  50 mL). The crude product was purified by column chromatography on silica gel using ethyl acetate/hexane (= 1/4) as an eluent to afford compound **M3** (0.86 g, 51%).

<sup>1</sup>H NMR (CDCl<sub>3</sub>, 300 MHz,  $\delta$ ): 7.92 (d, 4H), 6.94 (d, 4H), 4.02 (t, 4H), 1.80 (m, 4H), 4.00 (t, 4H), 1.35 (m, 12H), 0.96 (m, 6H). <sup>13</sup>C NMR (CDCl<sub>3</sub>, 300 MHz,  $\delta$ ): 14.00, 22.56, 25.61, 20.97, 31.50, 68.47, 114.71, 126.09, 132.35, 164.50, 196.40. HR-FAB MS *m/z* calcd for C<sub>26</sub>H<sub>30</sub>O<sub>4</sub> [M<sup>+</sup>]: 410.55; found: 410.5138.

#### Synthesis of 5,8-Dibromo-2,3-bis[4-(hexyloxy)phenyl]quinoxaline (**A1**)

A solution of 3,6-dibromo-1,2-benzenediamine (**M1**; 0.9 g, 3.6 mmol), 4,4'-dihexyloxybenzil (**M3**; 1.35 g, 3.6 mmol), and

*p*-TSA (0.12 g, 0.69 mmol) in ethyl alcohol (30 mL) was heated to reflux for 14 h. The solution was cooled to room temperature, and the reaction mixture was filtered to get the crude solid. After washing with cold ethanol, the product was purified by column chromatography on silica gel using dichloromethane/hexane (= 1/1) as an eluent to afford compound **A1** (0.3 mg, 51%).

$^1\text{H}$  NMR ( $\text{CDCl}_3$ , 300 MHz,  $\delta$ ): 7.84 (s, 2H), 7.64 (d, 4H), 6.87 (d, 4H), 3.99 (t, 4H), 1.79 (m, 4H), 1.36 (m, 12H), 0.91 (m, 6H).  $^{13}\text{C}$  NMR ( $\text{CDCl}_3$ , 300 MHz,  $\delta$ ): 160.43, 153.54, 138.97, 132.44, 131.63, 130.29, 123.40, 114.32, 68.05, 31.55, 29.13, 25.67, 22.57, 14.02. HR-FAB MS  $m/z$  calcd for  $\text{C}_{32}\text{H}_{36}\text{Br}_2\text{N}_2\text{O}_2$  [ $\text{M}^+$ ]: 638.1144; found: 638.1854.

#### Synthesis of 5,8-Dibromo-2,3-bis[4-(hexyloxy)phenyl]pyrido[3,4-*b*]pyrazine (**A2**)

A solution of 2,5-dibromopyridine-3,4-diamine (**M2**; 1.0 g, 3.7 mmol), 4,4'-dihexyloxybenzil (**M3**; 1.5 g, 3.7 mmol), and *p*-TSA (0.15 g, 0.7 mmol) in ethyl alcohol (30 mL) was heated to reflux for 16 h. The solution was cooled to room temperature, and the reaction mixture was filtered followed by washing with cold ethanol and purified by column chromatography on silica gel using dichloromethane/hexane (= 1/1) as an eluent to afford compound **A2** (1.2 g, 48%).

$^1\text{H}$  NMR ( $\text{CDCl}_3$ , 300 MHz,  $\delta$ ): 8.68 (s, 1H), 7.66 (t, 4H), 6.90 (d, 4H), 4.00 (t, 4H), 1.80 (m, 4H), 1.36 (m, 12H), 0.91 (m, 6H).  $^{13}\text{C}$  NMR ( $\text{CDCl}_3$ , 300 MHz,  $\delta$ ): 193.37, 164.33, 161.41, 132.16, 131.81, 131.53, 125.92, 114.55, 68.31, 31.36, 28.83, 25.46, 22.43, 13.88. HR-FAB MS  $m/z$  calcd for  $\text{C}_{31}\text{H}_{35}\text{Br}_2\text{N}_3\text{O}_2$  [ $\text{M}^+$ ]: 639.1096; found: 639.1710.

#### Synthesis of Poly{2,6-di-2-thienyl-4,8-bis(2'-ethylhexyloxy)-benzo[1,2-*b*:4,5-*b'*]dithiophene-*alt*-2,3-bis[4-(hexyloxy)phenyl]quinoxaline} (PBBDT-TBQ)

A mixture of 5,8-dibromo-2,3-bis[4-(hexyloxy)phenyl]quinoxaline (**A1**; 0.3 g, 0.46 mmol), bis(trimethyltin)-2,6-di-2-thienyl-4,8-bis(2'-ethylhexyloxy)-benzo[1,2-*b*:4,5-*b'*]dithiophene (0.4 g, 0.46 mmol), and  $\text{Pd}(\text{PPh}_3)_4$  (0.02 g) with toluene (15 mL) was heated under reflux for 72 h. After cooling to room temperature, the polymer was precipitated by slow dropwise addition of the reaction mixture into MeOH (250 mL), filtered off, and dried in air. The crude polymer was Soxhlet extracted subsequently with methanol, hexane, and chloroform. The chloroform fraction was concentrated by evaporation under reduced pressure and then precipitated in methanol. The precipitate was filtered off and dried to afford **PBBDT-TBQ** copolymer (0.29 g, 58%).

$^1\text{H}$  NMR ( $\text{CDCl}_3$ , 300 MHz,  $\delta$ ): 7.81–7.67 (br, 8.5 H), 6.97–6.90 (br, 7 H), 4.25–4.00 (br, 8 H), 1.82–1.74 (br, 10H), 1.41–1.25 (br, 18H), 1.06–0.94 (br, 24H). Anal. calcd (%) for ( $\text{C}_{71}\text{H}_{82}\text{N}_2\text{O}_4\text{S}_5$ ): C, 71.80; H, 6.96; N, 2.36; S, 13.5; found: C, 68.32; H, 6.78; N, 1.86; S, 14.18.

#### Synthesis of Poly{2,6-di-2-thienyl-4,8-bis(2'-ethylhexyloxy)-benzo[1,2-*b*:4,5-*b'*]dithiophene-*alt*-2,3-bis[4-(hexyloxy)phenyl]pyrido[3,4-*b*]pyrazine} (PBBDT-TPQ)

A mixture of 5,8-dibromo-2,3-bis[4-(hexyloxy)phenyl]pyrido[3,4-*b*]pyrazine (**A2**; 0.3 g, 0.46 mmol), bis(trimethyltin)-2,6-di-2-thienyl-4,8-bis(2'-ethylhexyloxy)-benzo[1,2-*b*:4,5-*b'*]dithiophene (0.4 g, 0.46 mmol), and  $\text{Pd}(\text{PPh}_3)_4$  (0.02 g) with toluene (15 mL) was heated under reflux for 72 h. After cooling to room temperature, the polymer was precipitated by slow dropwise addition of the reaction mixture into MeOH (250 mL), filtered off, and dried in air. The crude polymer was Soxhlet extracted subsequently with methanol, hexane, and chloroform. The chloroform fraction was concentrated by evaporation under reduced pressure and precipitated in methanol. The precipitate was filtered off and dried to afford **PBBDT-TPQ** copolymer (0.28 g, 55%).

$^1\text{H}$  NMR ( $\text{CDCl}_3$ , 300 MHz,  $\delta$ ): 7.79–7.74 (br, 6 H), 6.99–6.90 (br, 7 H), 4.20–4.06 (br, 8 H), 1.92–1.84 (br, 11H), 1.44–1.25 (br, 18H), 1.05–0.88 (br, 24H). Anal. calcd (%) for ( $\text{C}_{70}\text{H}_{81}\text{N}_3\text{O}_4\text{S}_5$ ): C, 70.73; H, 6.87; N, 3.35; S, 13.49; found: C, 70.58; H, 6.60; N, 2.50; S, 10.33.

#### Measurement and Characterization

All NMR spectra were recorded in deuterated chloroform ( $\text{CDCl}_3$ ) containing 0.003% TMS as an internal reference using a Bruker 300 spectrometer. Chemical shifts ( $\delta$ ), quoted in parts per million (ppm), and coupling constants ( $J$ ) were recorded in hertz (Hz). The molecular weight and molecular weight distribution of the copolymers were measured with a Waters gel permeation chromatography (GPC; Breeze system) using tetrahydrofuran (THF) as an eluent at 35 °C. The apparatus was equipped with two Waters Styragel columns (HR3 and HR4E), a refractive index detector (Waters 2414), and a dual-wavelength absorbance detector (Waters 2487). Polystyrene standards (Waters) were used for calibration. The absorption spectra were recorded on a Hitachi U-4100 spectrophotometer. Cyclic voltammetry (CV) was conducted on an Autolab PGSTAT 30 Electrochemical Workstation with glass carbon,  $\text{Ag}/\text{Ag}^+$ , and Pt wire as working electrode, reference electrode, and counter electrode, respectively, in a solution of 0.1 M tetrabutylammonium hexafluorophosphate ( $\text{Bu}_4\text{NPF}_6$ ) in deoxygenated acetonitrile ( $\text{CH}_3\text{CN}$ ) at a scan rate of 50  $\text{mV s}^{-1}$ . The redox potential of the polymer was corrected using the internal standard of  $\text{Fc}/\text{Fc}^+$  in  $\text{CH}_3\text{CN}$  (0.45 V vs.  $\text{Ag}/\text{Ag}^+$  electrode). Thermogravimetric analysis (TGA) and differential scanning calorimetry (DSC) measurements were performed under a nitrogen atmosphere at heating rates of 10 and 5  $^\circ\text{C min}^{-1}$  using a TA Instruments (TGA-Q500 and DSC-910S, respectively). Permanent dipole moment of dyes was calculated using the density functional theory (DFT) with Gaussian 09. Ground-state geometry optimization was performed using the B3LYP exchange correlation functional. The thickness of the active films was measured with a depth-profile meter (Veeco Dektak 150, USA). Five lines on a film of 1 cm  $\times$  1 cm were made by carefully scratching with a plastic tip, and the average height between the hills and valleys is used to represent the film thickness. GIXRD patterns

were collected using a Rigaku-TTRAX III diffractometer, operating at an accelerating voltage of 50 kV and current of 300 mA. A Ni-filtered Cu K $\alpha$  radiation source (0.154 nm) was used. A 0.4° incident angle, a 0.01° sampling step, a 5° min<sup>-1</sup> scanning rate, and 2 $\theta$  of ~3°–40° of scanning range were carefully chosen to allow for complete X-ray penetration into the polymer film. AFM measurements were performed using PeakForce tapping mode with PeakForce Quantitative Nanomechanical Mapping software (Bruker). The set point of the PeakForce applied during the measurements was in the range of a few nanonewtons; the PeakForce frequency was 2 kHz. The PeakForce error imaging technique represents the feedback signal that controls the Z piezo in the PeakForce tapping mode and is equivalent to the deflection error in contact mode or amplitude error in tapping mode. These feedback signals are often used to create 3D images which help to visualize the topography. Hole mobility was measured according to a method based on the space charge-limited current (SCLC) model described in the literature,<sup>36,37</sup> using a diode configuration of ITO/PEDOT:PSS/polymer: PC<sub>71</sub>BM/Pd. The SCLC current was measured under dark conditions using a Keithley Model 2400 unit. Femtosecond time-resolved photoluminescence (FTR-PL) was then conducted by the sum-frequency technique (FluoMax, IB Photonics Ltd.) along with the instrument response function (IRF) of 150 fs, and the excitation wavelength was 420 nm. To prevent laser-induced thermal effects, the diameter of the spot size on the sample was increased to 300  $\mu$ m, and the excitation power was reduced to 4 mW. Furthermore, to resolve the exciton dynamics, the time-dependent photoluminescence was fitted in an appropriate exponentially decaying function.<sup>38</sup>

### Solar Cell Device Fabrication and Characterization

The inverted PSCs were fabricated with the device structure of ITO/ZnO (40 nm)/poly[(9,9-dioctyl-2,7-fluorene)-*alt*-(9,9-bis(3'-(*N,N*-dimethylamino)propyl)-2,7-fluorene)] (PFN) (5 nm)/polymer: PC<sub>71</sub>BM (65–80 nm)/MoO<sub>3</sub> (8 nm)/Ag (100 nm). Prior to use, patterned ITO-coated glass substrates (10  $\Omega$ /square) were successively cleaned by ultrasonication in 1% neutral detergent in water, then deionized water, followed by acetone, and finally isopropanol for 10 min each and subsequently dried under a stream of dry nitrogen. The substrates then underwent UV–ozone treatment for 10 min prior to the deposition of a ~40-nm-thick layer of ZnO. The ZnO precursor was prepared using zinc acetate dehydrate [Zn(CH<sub>3</sub>COO)<sub>2</sub>·2H<sub>2</sub>O, 99.999%; Aldrich] as starting material, and 2-ethoxyethanol and monoethanolamine (MEA, 99.7%; Aldrich) as the nontoxic solvent and stabilizer, respectively, under vigorous stirring for 12 h for the hydrolysis reaction in air. The respective solutions were spin-coated on ITO-coated glass substrates at 5000 rpm for 30 s and preheated at 180 °C for 30 min in air to remove residual organic materials and then transferred into an inert N<sub>2</sub>-filled glove box (<0.1 ppm O<sub>2</sub> and H<sub>2</sub>O). Subsequently, PFN interfacial layer was spin-casted onto the active layer according to a similar method described in the literature.<sup>20</sup> Blend solutions were prepared by dissolving the target polymer (PBDT-TBQ or PBDT-TPQ) and PC<sub>71</sub>BM (purchased from Nano-C) in *o*-DCB solution in the blend ratios of 1:1 and 1:2 with a polymer concentration of 12 mg mL<sup>-1</sup> and were heated to 100

°C and stirred 8 h for complete dissolution. Then, the blend solution with 3 vol % 1,8-diiodooctane (DIO) additive was spin-casted. The wet film was slowly dried in a covered Petri dish for 3 h in the glove box and then annealed at 110 °C for 10 min. Afterward, methanol was dropped onto the active layer with a spin-casting rate at 2000 rpm for 60 s, and subsequently, the coated substrates were transferred to a thermal evaporator and evacuated to  $\leq 5 \times 10^{-6}$  Torr. Molybdenum oxide was thermally deposited on top of the active layer with an evaporation rate of 0.1 Å s<sup>-1</sup>. Ultimately, 100-nm silver film was deposited on top of the molybdenum oxide layer through a shade mask. The *J*-*V* curves were measured using a Keithley 4200 source-measuring unit. A calibrated solar simulator (Oriel) with a 100 mW cm<sup>-2</sup> power density was used as the light source. An IPCE (QE-R3011) characterization platform supplied by Enlitech was used for data acquirement. All IPCE spectra were recorded using a lock-in technique at a chopping frequency of 100 Hz.

## RESULTS AND DISCUSSION

### Synthesis and Characterization

Scheme 1 outlines the chemical structure and the synthetic route for the two copolymers by Stille cross-coupling reactions under thermal heating conditions using Pd(PPh<sub>3</sub>)<sub>4</sub> as a catalyst. Crude polymers were purified by Soxhlet extraction with methanol, hexane, and chloroform.

The chloroform solution was concentrated, and the product was reprecipitated in methanol to obtain the target copolymers. The <sup>1</sup>H NMR spectra of the synthesized copolymers showed a general broadening when compared with those of the monomers, as depicted in the spectrum of PBDT-TBQ (Fig. 1) and PBDT-TPQ (Fig. 2). The number-average molecular weights (*M*<sub>n</sub>s) of the synthesized PBDT-TBQ and PBDT-TPQ polymers were determined by GPC against polystyrene standards in a THF eluent and were found to be as 10.13 and 10.95 kDa, with polydispersity indices of 1.6 and 1.9, respectively.

The thermal properties of the polymers were determined by TGA under a nitrogen atmosphere at a heating rate of 10 °C min<sup>-1</sup> as shown in Supporting Information Figure S1. Both polymers are thermally stable with onset decomposition temperatures at 5% weight loss (*T*<sub>d</sub>) above 300 °C, which indicates that the thermal stability of the study copolymers is adequate for application in optoelectronic devices. Additionally, these target polymers show neither glass transition temperature nor melting point in the DSC curves of the second heating and cooling runs, suggesting that the rigid backbones of these copolymers limit the chain motion.

### Optical and Electrochemical Properties

UV–visible absorption spectra together with energy-level diagram of the study polymers of PBDT-TBQ and PBDT-TPQ are displayed in Figure 3, and the relevant data are summarized in Table 1. The absorption spectra of the polymers [Fig. 3(a)] show two distinct absorption bands. The short-wavelength absorption bands below 430 nm are assigned to

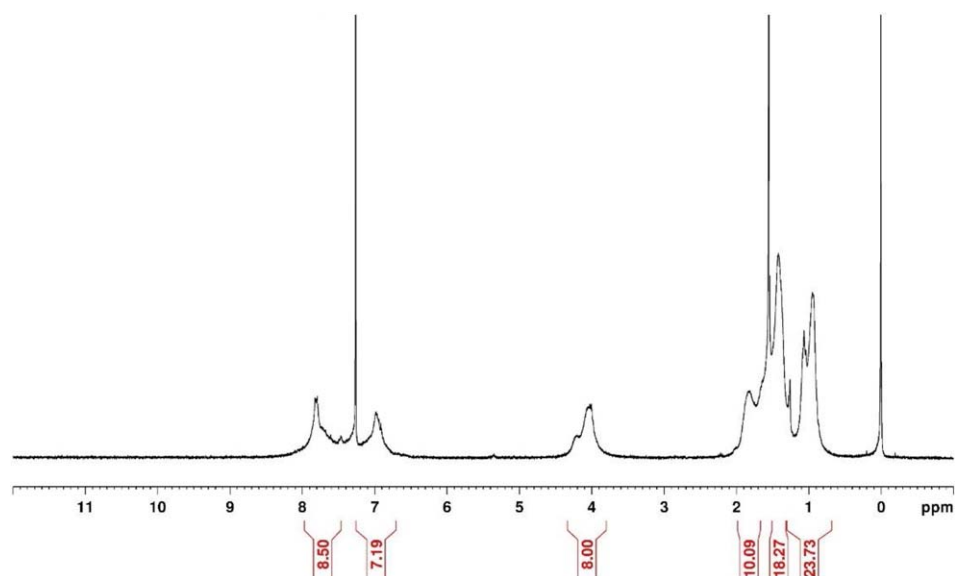


**FIGURE 1**  $^1\text{H}$  NMR spectra (300 MHz) of PBDT-TBQ in  $\text{CDCl}_3$ . [Color figure can be viewed in the online issue, which is available at [wileyonlinelibrary.com](http://wileyonlinelibrary.com).]

a delocalized excitonic  $\pi$ - $\pi^*$  transition in the conjugated main chains, whereas the long-wavelength absorption bands at around 500–620 nm are reasonably ascribed to the strong internal charge transfer interaction between the electron-donating and electron-accepting units in the polymer backbone. The PBDT-TBQ and BDT-TPQ solutions show their maximum absorptions at 405 and 530 nm and 415 and 575 nm, respectively, whereas those of the corresponding polymer films shift to the longer wavelength region and show maximum absorptions at 414 and 558 nm and 426 and 590 nm, respectively, indicating intramolecular and/or intermolecular interactions existing in the solid state. The optical bandgap ( $E_g^{\text{opt}}$ ) deduced from the absorption edges

of the thin film spectra are in the following order: PBDT-TPQ (1.69 eV) < PBDT-TBQ (1.81 eV). Furthermore,  $\lambda_{\text{max}}$  of PBDT-TPQ film is red-shifted by 32 nm when compared with that of PBDT-TBQ, indicating the pyrido-substituted quinoxaline PQ unit offering stronger electron-withdrawing capacity than the benzo-substituted quinoxaline BQ analog. Such significantly enhanced absorption in the red region may uplift the exciton formation as the solar flux peaks are here. In addition, PBDT-TPQ film displays a vibronic shoulder at  $\sim 650$  nm, indicating that there exists some ordered structural organization in the solid state,<sup>39</sup> which should benefit the charge mobility and photovoltaic performance of the polymer.

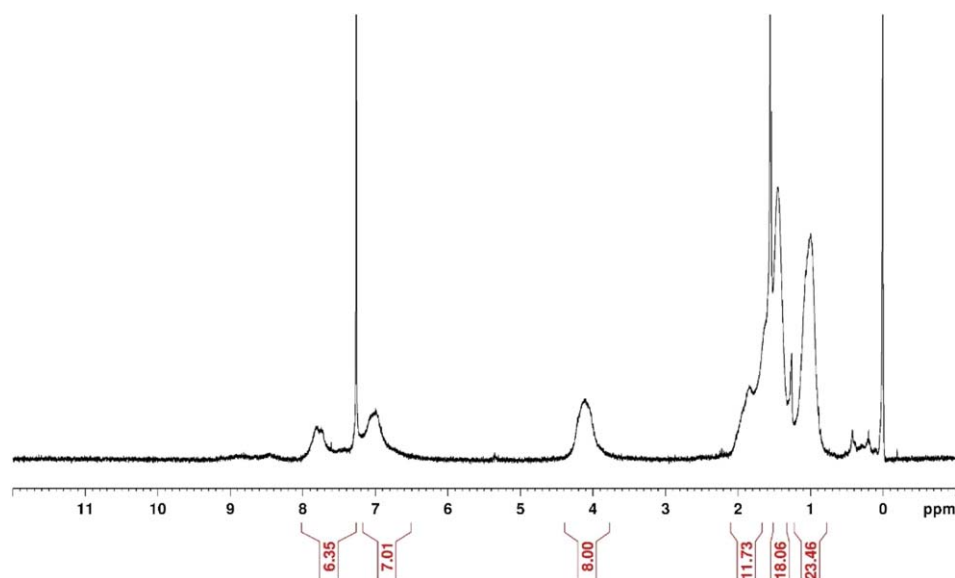


**FIGURE 2**  $^1\text{H}$  NMR spectra (300 MHz) of PBDT-TPQ in  $\text{CDCl}_3$ . [Color figure can be viewed in the online issue, which is available at [wileyonlinelibrary.com](http://wileyonlinelibrary.com).]

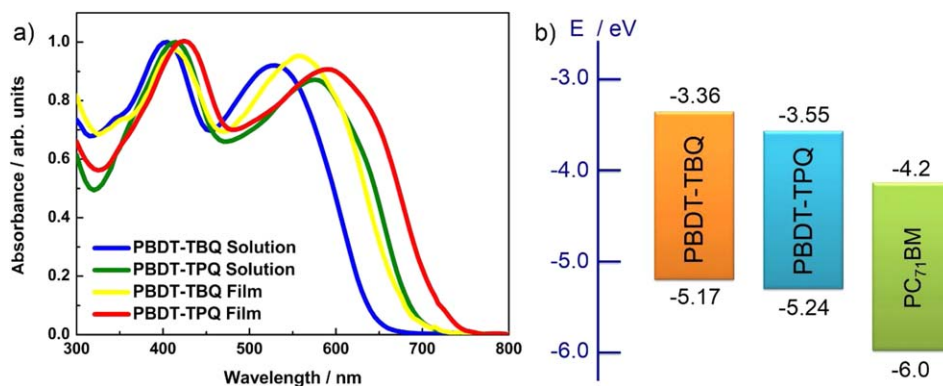


**FIGURE 3** (a) UV-vis absorption spectra of PBBDT-TBQ and PBBDT-TPQ in chloroform solution and as thin films. (b) Energy-level diagram of the active layer components. [Color figure can be viewed in the online issue, which is available at [wileyonlinelibrary.com](http://wileyonlinelibrary.com).]

Cyclic voltammetry was used to evaluate the electrochemical properties and to estimate the energy levels of the polymers. The HOMO levels were estimated from the onsets of their corresponding oxidative peaks (Supporting Information Fig. S2). The LUMO levels were then calculated from the differences between the HOMO energy level and the optical bandgaps. Figure 3(b) depicts a sketch of the energy levels for PBBDT-TBQ, PBBDT-TPQ, and [6,6]-phenyl-C<sub>71</sub>-butyric acid methyl ester (PC<sub>71</sub>BM). PBBDT-TPQ exhibits a relatively lower-lying HOMO energy level at  $-5.24$  eV, which is in an ideal range to ensure better air stability and can be anticipated to produce a higher open-circuit voltage ( $V_{oc}$ ), in accordance with the known linear correlation of  $V_{oc}$  with the difference between the HOMO energy level of a donor and the LUMO energy level of an acceptor. The LUMO energy levels of these two polymers are all located within a suitable range from  $-3.36$  to  $-3.55$  eV and are clearly higher-lying than that of PC<sub>71</sub>BM, providing sufficient driving force for charge separation and electron transfer without too much energy loss.

To evaluate the impact of the different acceptors on the molecular structures and electronic properties, theoretical calculations by DFT model at the B3LYP/6-31G\* level were performed on trimers. As the side-chain substituents have little influence on the oxidative and reductive properties of the molecule, the alkyl side chains were all truncated to methyl groups for simplicity. The wave functions of the frontier molecular orbital of model compounds are depicted in Figure 4. As can be observed, the electron density in the HOMO wave function is mostly delocalized along the whole polymer backbone,

whereas the electron density associated with the LUMO is fairly well localized at the electron acceptor site. Additionally, in LUMO wave function, PBBDT-TPQ appears to be more efficient in intracharge transfer than that of PBBDT-TBQ. The average torsion angles of PBBDT-TBQ between D- $\pi$  and  $\pi$ -A repeat units are of  $8.1^\circ$  and  $23.5^\circ$ , respectively, whereas the average torsion angles of PBBDT-TPQ between D- $\pi$  and  $\pi$ -A repeat units decrease to  $7.9^\circ$  and  $20.3^\circ$ , respectively. DFT calculations of the ground state of the polymers show the permanent dipole moment of 3.95 and 5.83 debyes for PBBDT-TBQ and PBBDT-TPQ, respectively. The slightly higher coplanarity of PBBDT-TPQ may result from the higher dipole moment, which can induce strong intermolecular interaction (see Supporting Information Fig. S3).

### Evaluation of Charge Carrier Mobility and Photovoltaic Properties

The hole mobility of PBBDT-TBQ and PBBDT-TPQ was measured by SCLC method. PBBDT-TPQ demonstrates a relatively higher hole mobility of  $1.4 \times 10^{-5} \text{ cm}^2 \text{ V}^{-1} \text{ s}^{-1}$  and is nearly four times higher than that of the PBBDT-TBQ ( $3.3 \times 10^{-6} \text{ cm}^2 \text{ V}^{-1} \text{ s}^{-1}$ ; Supporting Information Fig. S4). This variation in the charge transport behavior can be attributed to the relatively ordered structure and stronger intermolecular interactions of PBBDT-TPQ polymer as proven by synchrotron grazing incidence wide-angle X-ray scattering (GIWAXS) analysis [Fig. 5(a,b)], thereby enabling crystalline ordering and good uniformity in the molecular conformation. As expected, the higher hole mobility of PBBDT-TPQ yielded a balanced charge carrier transport in the active layer, which is expected

**TABLE 1** Optical and Electrical Characteristics of the Target Polymers

Polymer	$\lambda_{\text{max}}$ (nm)		$\lambda_{\text{edge}}$ (nm)	$E_{\text{g}}^{\text{opt}}$ (eV) <sup>a</sup>	$E_{\text{HOMO}}$ (eV) <sup>b</sup>	$E_{\text{LUMO}}$ (eV) <sup>c</sup>	$T_{\text{d}}$ (°C) <sup>d</sup>
	Solution	Film	Film				
PBBDT-TBQ	405, 530	414, 558	685	1.81	$-5.17$	$-3.36$	329
PBBDT-TPQ	415, 575	426, 590	734	1.69	$-5.24$	$-3.55$	325

<sup>a</sup> Estimated from the optical absorption edge in thin films.

<sup>b</sup> Estimated from the onset of the oxidation peaks of cyclic voltammogram.

<sup>c</sup> Values deducted from  $E_{\text{HOMO}}$  and optical bandgap.

<sup>d</sup> Decomposition temperature (5% weight loss) determined by thermogravimetric analysis under nitrogen.

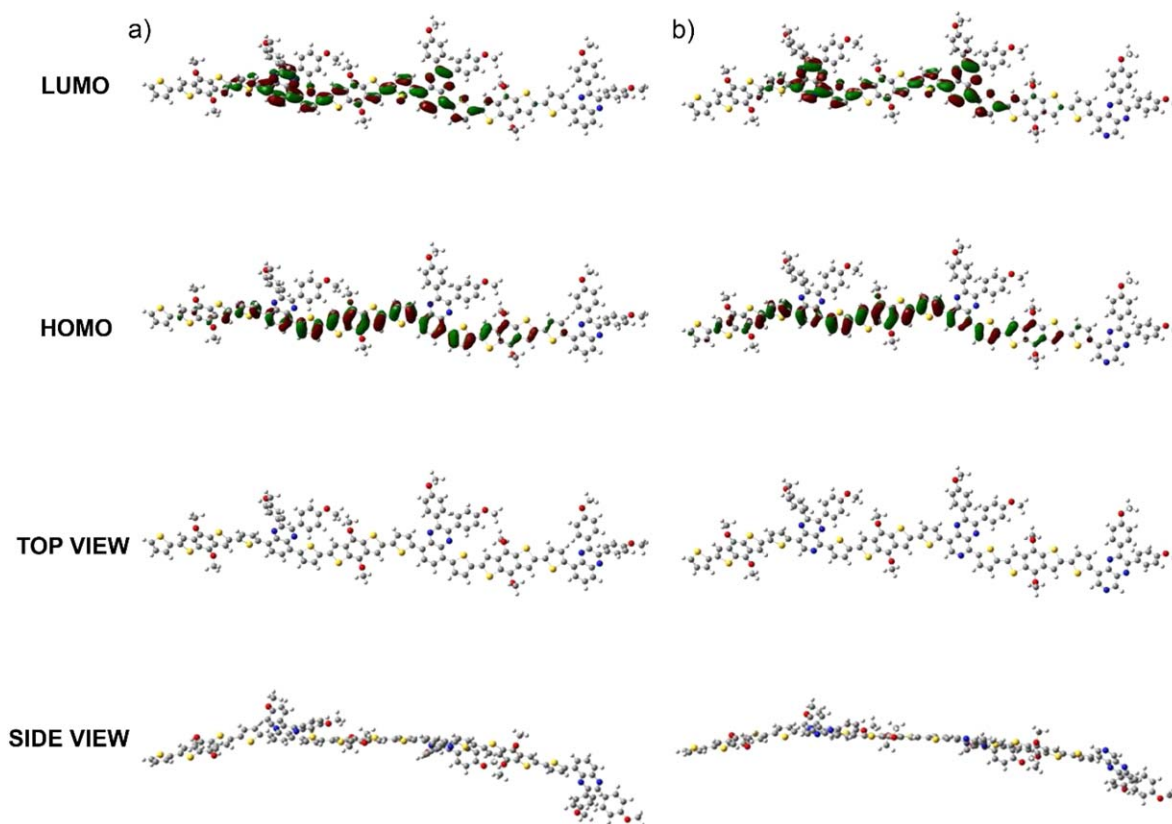


**FIGURE 4** Minimum energy conformations of optimized geometries of (a) PBDT-TBQ and (b) PBDT-TPQ trimers. Gaussian optimized at B3LYP/6-31G\* level with visualization of the corresponding HOMO/LUMO energy distributions. Color code: gray (C), white (H), red (O), blue (N), and yellow (S). [Color figure can be viewed in the online issue, which is available at [wileyonlinelibrary.com](http://wileyonlinelibrary.com).]

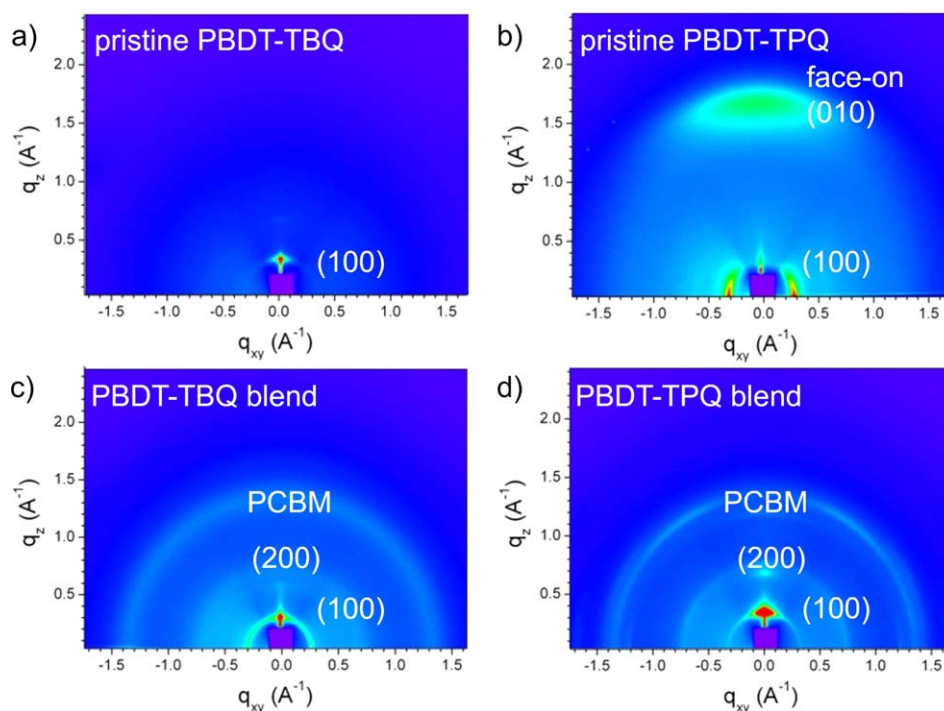


**FIGURE 5** Two-dimensional grazing incidence wide-angle X-ray scattering (GIWAXS) patterns of (a) PBDT-TBQ, (b) PBDT-TPQ neat films, (c) PBDT-TBQ:PC<sub>71</sub>BM (1:1), and (d) PBDT-TPQ:PC<sub>71</sub>BM (1:2) blend films. [Color figure can be viewed in the online issue, which is available at [wileyonlinelibrary.com](http://wileyonlinelibrary.com).]

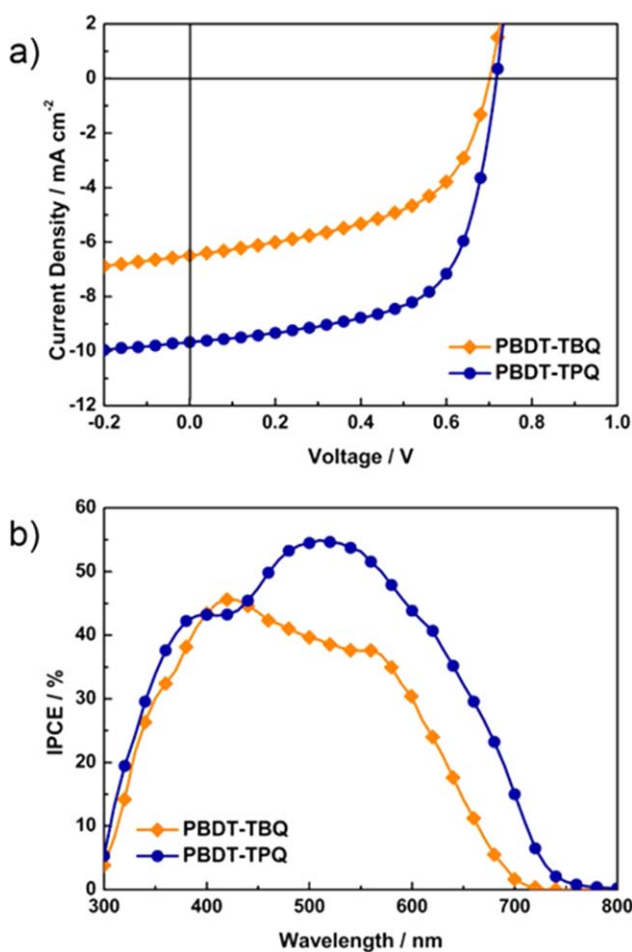


**FIGURE 6** (a)  $J$ - $V$  curves of optimized devices based on 1:1 PBDT-TBQ:PC<sub>71</sub>BM and 1:2 PBDT-TPQ:PC<sub>71</sub>BM solar cells under AM 1.5G solar illumination, and (b) the corresponding IPCE spectra of optimized devices illuminated by monochromatic light. Legend: orange diamonds (◆) represent the PBDT-TBQ device ( $V_{oc} = 0.70$  V,  $J_{sc} = -6.50$  mA cm<sup>-2</sup>, FF = 53.8%, and PCE = 2.45%), and royal blue circles (●) represent the PBDT-TPQ device ( $V_{oc} = 0.72$  V,  $J_{sc} = -9.69$  mA cm<sup>-2</sup>, FF = 63.1%, and PCE = 4.40%). [Color figure can be viewed in the online issue, which is available at [wileyonlinelibrary.com](http://wileyonlinelibrary.com).]

to contribute in part, not just to the higher short-circuit current density ( $J_{sc}$ ) but also to higher fill factor (FF) and overall better device performance elaborated below.

To gain deeper insight into the molecular packing and nanostructural order within the active layer, GIWAXS analysis was performed to examine the neat PBDT-TBQ and PBDT-TPQ films as well as the optimized 1:1 PBDT-TBQ:PC<sub>71</sub>BM and 1:2 PBDT-TPQ:PC<sub>71</sub>BM blend films. In Figure 5(a), the 2D GIWAXS pattern of the neat PBDT-TBQ film shows an anisotropic ring-scattering pattern at  $q = 0.34$  Å<sup>-1</sup> with an interlayer  $d_{100}$  spacing of 18.52 Å, corresponding to the periodic lamellae of polymer backbones. In contrast, the neat PBDT-TPQ film [Fig. 5(b)] shows arc and anisotropic ring-scattering patterns. The Bragg scattering peak of (100) appears at  $q = 0.31$  Å<sup>-1</sup> with an interlayer  $d_{100}$  spacing of 20.06 Å, whereas a distinctive arc scatter-

ing along the  $q_z$  axis at  $q = 1.64$  Å<sup>-1</sup> represents the (010) face-on  $\pi$ - $\pi$  stacking packing reflection peak of the polymer backbones ( $d_{\pi-\pi} = 3.84$  Å). These results manifest that the PBDT-TPQ film possesses a relatively ordered structure and stronger intermolecular interactions, which can be supported by the observation in the UV-vis absorption spectra [Fig. 3(a)], where the PBDT-TPQ film shows a distinct vibronic shoulder in the long wavelength.<sup>39</sup> On adding PC<sub>71</sub>BM in PBDT-TBQ and PBDT-TPQ blend systems, both GIWAXS patterns show a new isotropic broad reflection at  $q = 1.34$  Å<sup>-1</sup> due to scattering from the PC<sub>71</sub>BM domains. Furthermore, an additional (200) reflection peak can be clearly observed, indicating that lamellar stacking of the blend film has further been improved [Fig. 5(c,d)]. The result may arise from the strong polymer-fullerene interactions that delay the fullerene self-assembly in the final drying process. Therefore, fullerene aggregation during film formation may promote the self-organization of the polymer.<sup>40,41</sup>

To characterize the photovoltaic properties of PBDT-TBQ and PBDT-TPQ, inverted BHJ PSCs with a device configuration of ITO/ZnO (40 nm)/PFN (5 nm)/polymer:PC<sub>71</sub>BM/MoO<sub>3</sub> (8 nm)/Ag (100 nm) were fabricated and examined under simulated 100 mW cm<sup>-2</sup> AM 1.5G illumination. The incorporation of a thin PFN cathode interlayer can construct interfacial dipole, which could result in the reduced electron injection barrier and enhanced built-in potential across the device.<sup>20,27,32</sup> The optimized polymer to PC<sub>71</sub>BM ratios of PBDT-TBQ and PBDT-TPQ used to form the active layers of the PSCs were 1:1 and 1:2, respectively. The polymer active layers of PBDT-TBQ and PBDT-TPQ were spin-coated from *o*-DCB solutions with 3 vol % DIO additives. DIO is commonly used as a solvent additive in PSCs to improve the device performances owing to its high boiling point (363 °C) and good solubility for fullerene aggregates to form favorable nanostructures. We optimized the thickness of the active layers and found that 65–80 nm was the best thickness for all devices. Figure 6(a) shows the  $J$ - $V$  curves of the champion PSC for PBDT-TBQ:PC<sub>71</sub>BM- and PBDT-TPQ:PC<sub>71</sub>BM-based devices. The optimal photovoltaic parameters of the devices are summarized in Table 2. In the optimized 1:2 PBDT-TPQ:PC<sub>71</sub>BM device with thermal annealing at 110 °C for 10 min, the  $V_{oc}$  reaches to 0.72 V with a  $J_{sc}$  of 9.69 mA cm<sup>-2</sup> and an FF of 63.1%, offering a PCE of 4.40%. Conversely, the device based on optimized 1:1 PBDT-TBQ:PC<sub>71</sub>BM exhibits an inferior PCE of 2.45%, with a  $V_{oc}$  of 0.70 V, a  $J_{sc}$  of 6.50 mA cm<sup>-2</sup>, and an FF of 53.8%, presumably due to the inefficient exciton dissociation

**TABLE 2** Photovoltaic Parameters of Optimized Solar Cells

Polymer	Polymer: PC <sub>71</sub> BM	$V_{oc}$ (V)	$J_{sc}$ (mA cm <sup>-2</sup> )	FF (%)	PCE <sup>a</sup> (%)
PBDT-TBQ	1:1	0.70	6.50	53.8	2.45 (2.28)
PBDT-TBQ	1:2	0.68	5.12	51.7	1.80 (1.57)
PBDT-TPQ	1:1	0.72	8.26	54.7	3.25 (3.09)
PBDT-TPQ	1:2	0.72	9.69	63.1	4.40 (4.28)

<sup>a</sup> Average PCE of more than 20 optimized devices in parentheses.

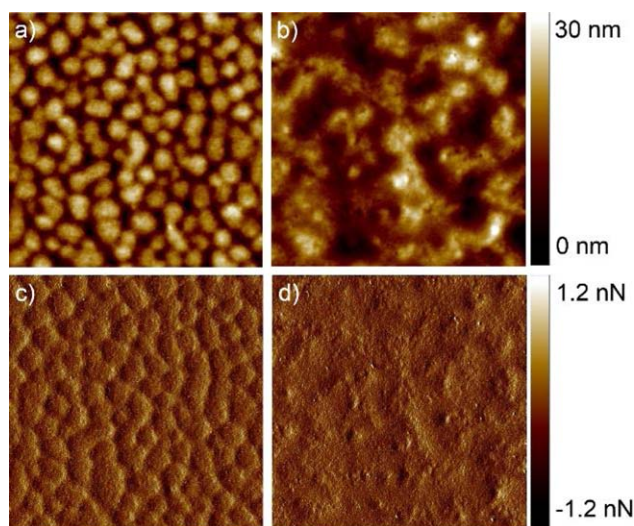


**FIGURE 7** Morphology characterization of PeakForce tapping-mode atomic force microscopy topographic images (upper row) and PeakForce error images (lower row) of 1:1 PBDT-TBQ:PC<sub>71</sub>BM blend films with 3 vol % DIO [Panels (a) and (c)] and 1:2 PBDT-TPQ:PC<sub>71</sub>BM blend films with 3 vol % DIO [Panels (b) and (d)]. The imaging size is 2 μm × 2 μm for each panel. [Color figure can be viewed in the online issue, which is available at [wileyonlinelibrary.com](http://wileyonlinelibrary.com).]

and low carrier mobility. Further increase of the fullerene ratio in PBDT-TBQ:PC<sub>71</sub>BM blends yielded negative effect in both  $J_{sc}$  and FF, which resulted in a decreased PCE. As expected from the low-lying HOMO energy levels of the polymers, the trend in  $V_{oc}$  agrees well with the electrochemical potentials. Note that PBDT-TPQ-based devices show dramatically higher  $J_{sc}$  and FF than those of PBDT-TBQ-based devices. The reasons can be attributable to the better backbone coplanarity, enhancing absorption in the long wavelength region, optimal morphology with proper domain size of the active layer, and higher charge carrier mobility that can promote the exciton separation and charge transport, as well as enhanced charge collection efficiency. The moderate PCE may be attributed to a lower molecular weight as observed in other studies.<sup>15,42,43</sup> Nevertheless, the better device performance of PBDT-TPQ over that of PBDT-TBQ clearly suggests that the newly developed PQ acceptor unit is better than the widely used BQ acceptor unit to construct highly efficient PSCs.

To evaluate the photoresponse of PBDT-TBQ and PBDT-TPQ and to calibrate the  $J_{sc}$  data, the corresponding IPCE spectra of the devices elaborated above were measured under illumination of monochromatic light [Fig. 6(b)]. When compared with the absorption spectra of the pristine polymers, the conspicuously broadened IPCE responses in the visible region can be attributed to both the intrinsic absorptions of the polymers and the response of PC<sub>71</sub>BM. In the IPCE spectra, PBDT-TPQ blend exhibits a very broad panchromatic spectrum over the entire excitation spectral range with relatively high IPCE values above 50% in the 458–572 nm range. The integrated  $J_{sc}$  values from the IPCE spectra are 6.10 and

8.92 mA cm<sup>-2</sup> for PBDT-TBQ and PBDT-TPQ devices, respectively. The  $J_{sc}$  values calculated from the integration of the IPCE spectra are within a 5% error, which agrees well with those obtained from the  $J$ - $V$  measurements, supporting the reliability of the photovoltaic measurement.

To better understand the morphological effect of the optimized active layers on the OPV performance, we investigated the morphological discrepancies of the polymer:PC<sub>71</sub>BM blends by PeakForce tapping-mode atomic force microscopy. Figure 7 shows the topographic and PeakForce error images of the best performing active films on 1:1 PBDT-TBQ:PC<sub>71</sub>BM and 1:2 PBDT-TPQ:PC<sub>71</sub>BM blends. The topography of these two active films is prominently different. PBDT-TBQ:PC<sub>71</sub>BM blend film clearly exhibits a quite large spherical domain (~100 nm) with a root-mean-square (rms) surface roughness of 3.5 nm. The relatively larger globular clusters and poorly formed bicontinuous percolation pathways result in the geminate recombination, limited charge transport, and/or collection processes, as confirmed by the low charge mobility, photocurrent, and FF of the corresponding devices.<sup>2,3</sup> In marked contrast, the surface of PBDT-TPQ:PC<sub>71</sub>BM blend film is extremely uniform in height with an rms value of 2.2 nm. The long well-defined nanoscale phase separations can be seen more clearly, which is beneficial to efficient exciton dissociation at the D/A interfaces and efficient charge carrier transport to the electrodes.<sup>2,3</sup> This may be attributable to the fact that the polar nitrogen atom in the PQ moiety may possess better interaction with PCBM when compared with the nonpolar BQ moiety. These results could demonstrate the merit of using PQ as an acceptor subunit in the D-A polymer to some extent.

To address the exciton lifetime and charge carrier dynamics of the neat and polymer blend films, FTR-PL was then conducted along with the IRF of 150 fs, and the excitation wavelength was 420 nm. The broadband exciton dynamics of the PBDT-TBQ and PBDT-TPQ dissolved in THF are shown in Figure 8. The spectral width of the PBDT-TPQ solution is narrower when compared with that of PBDT-TBQ solution, indicating that the molecular structure of PBDT-TPQ is more coplanar than that of PBDT-TBQ.

Figure 9(a) depicts the dynamics of the FTR-PL for the pristine PBDT-TBQ and PBDT-TPQ films with various emission peak wavelengths. To acquire the relaxation time, the experimental results were fitted in a two-constant exponentially decaying function as follows:

$$I_{PL} = A_{ee}e^{-t/\tau_{ee}} + A_e e^{-t/\tau_e}, \quad (1)$$

where  $A_{ee}$  is the amplitude for the exciton–exciton annihilation,  $A_e$  is the amplitude for exciton,  $\tau_{ee}$  is the time constant of the exciton–exciton annihilation, and  $\tau_e$  is the exciton lifetime. The exciton lifetimes for the pristine PBDT-TBQ and PBDT-TPQ films are 712 ps and 491 ps, respectively (see Table 3), which are inversely proportional to the exciton binding energy (the energy for the exciton to dissociate in the polymer blends). To gain a deeper insight into the origin of IPCE of PBDT-TBQ- and PBDT-TPQ-based solar cells, PL

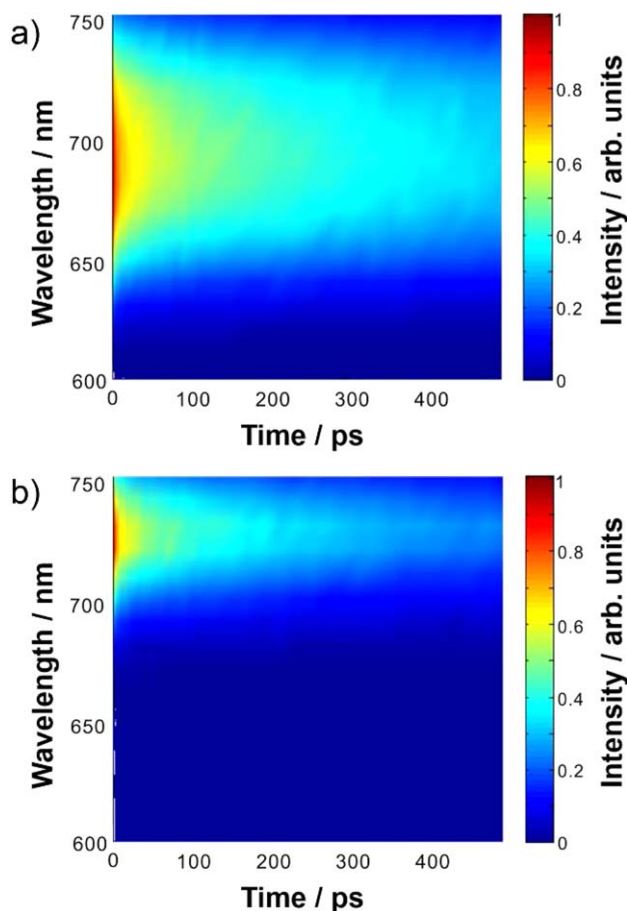


**FIGURE 8** Broadband time-resolved photoluminescence. The pulse duration, repetition rate, and average power of the excitation are 100 fs, 80 MHz, and 4 mW, respectively: (a) PBDT-TBQ polymer and (b) PBDT-TPQ polymer dissolved in THF. [Color figure can be viewed in the online issue, which is available at wileyonlinelibrary.com.]

quenching experiments were performed for the blend films, and the exciton dissociation at the region of charge transfer radius<sup>44</sup> was also calculated. The PL spectra of PBDT-TBQ:PC<sub>71</sub>BM and PBDT-TPQ:PC<sub>71</sub>BM blends [Fig. 9(b)] at the initial time ( $t = 0.5$  ps) infer that the photo-excited electrons in PBDT-TBQ and PBDT-TPQ originally relax to a lower meta-stable state via a rapid electron-phonon interaction (thermal relaxation). In this meta-stable state, the main exciton dissociation can be conspicuously observed at the emission wavelengths of 650 and 700 nm for the PBDT-TBQ:PC<sub>71</sub>BM and PBDT-TPQ:PC<sub>71</sub>BM blends, respectively.

PL dynamics of the pristine and polymer blend films are shown in Figure 10. To obtain the relaxation time, the experimental results were fitted into a two-constant exponentially decaying function as follows:<sup>45</sup>

$$I_{\text{PL}} = Ae^{-t/\tau} + A_e e^{-t/\tau_e}, \quad (2)$$

where  $A$  is the amplitude for the exciton-exciton annihilation or the exciton dissociation;  $A_e$  is the amplitude for the exci-

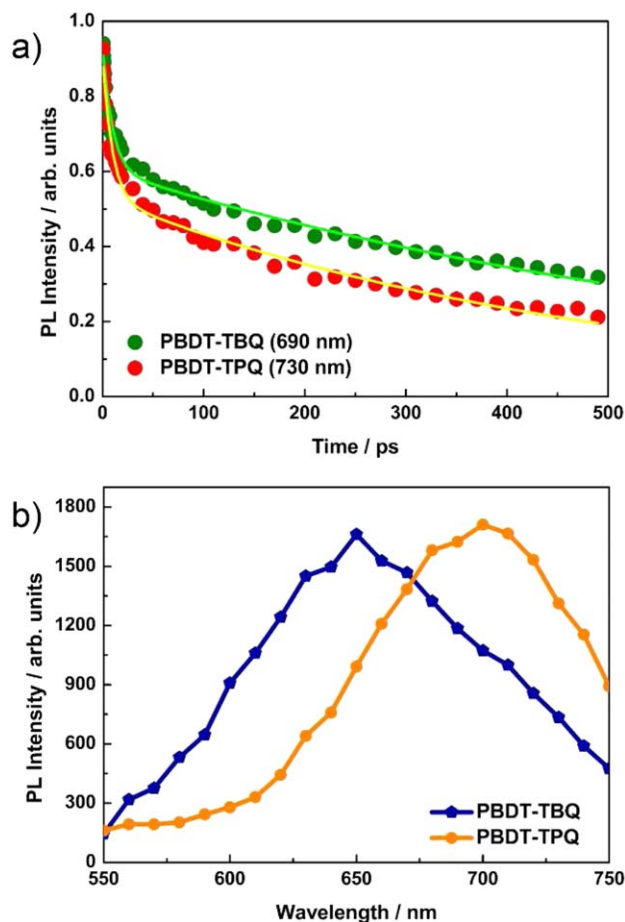


**FIGURE 9** (a) Normalized time-resolved photoluminescence intensities of PBDT-TBQ and PBDT-TPQ polymers dissolved in THF at the maximum peak wavelength. (b) Transient photoluminescence spectra of PBDT-TBQ:PC<sub>71</sub>BM and PBDT-TPQ:PC<sub>71</sub>BM blend films along with the excitation wavelength of 420 nm and the initial time of 0.5 ps. [Color figure can be viewed in the online issue, which is available at wileyonlinelibrary.com.]

ton diffusion;  $\tau$  is the time constant of the exciton-exciton annihilation or the exciton dissociation; and  $\tau_e$  is the exciton diffusion lifetime. The corresponding data are also summarized in Table 4. For the neat PBDT-TBQ and PBDT-TPQ films, the trends in the exciton lifetimes are similar to those of the solution obtained from the FTR-PL results. In addition, similar time constants (0.62 and 0.67 ps, within the experimental error) of the exciton dissociation are also obtained for these two blends because of the balanced competition between the built-in driving force in the charge transfer radius and the exciton mobility. It is noteworthy that the addition of PC<sub>71</sub>BM reduces the exciton diffusion lifetime in the PBDT-

**TABLE 3** Decay Parameters of Target Polymers in THF Solutions

Polymer	$A_1$ (%)	$\tau_{ee}$ (ps)	$A_2$ (%)	$\tau_e$ (ps)
PBDT-TBQ	35	9.74	65	712
PBDT-TPQ	41	9.56	59	491

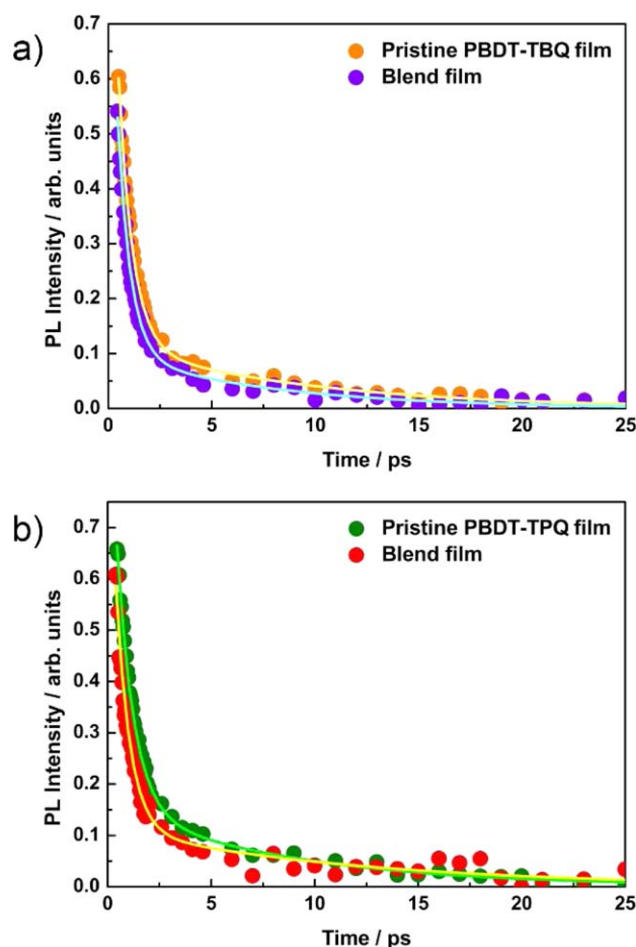


**FIGURE 10** Photoluminescence quenching characteristics of (a) the pristine PBDT-TBQ and PBDT-TBQ:PC<sub>71</sub>BM blend film and (b) the pristine PBDT-TPQ and PBDT-TPQ:PC<sub>71</sub>BM blend film. [Color figure can be viewed in the online issue, which is available at [wileyonlinelibrary.com](http://wileyonlinelibrary.com).]

TBQ owing to the built-in driving force in the region of charge transfer radius. Conversely, the exciton diffusion lifetime in PBDT-TPQ is extended from 8.67 to 11.74 ps with the addition of PC<sub>71</sub>BM, which is beneficial for the exciton dissociation. It seems that the addition of PC<sub>71</sub>BM appears to improve the crystallinity of the PBDT-TPQ blend to some extent and quite likely is responsible for the differences in exciton lifetime of these two polymer blends. Moreover, the efficiency of the exciton dissociation in the region of charge transfer radius can be evaluated from the following equation:

$$\eta = (1/\tau) / (1/\tau + 1/\tau_e),$$

where  $\tau$  is the exciton dissociation time and  $\tau_e$  is the exciton diffusion lifetime. The experimental data show that the exciton dissociation efficiency is better in the PBDT-TPQ:PC<sub>71</sub>BM blend ( $\eta = 94.6\%$ ) than that in the PBDT-TBQ:PC<sub>71</sub>BM blend ( $\eta = 92.5\%$ ), which can be used to explain that the IPCE spectra of the PBDT-TPQ-based OPV ( $\sim 41\%$ ) is higher than that of the PBDT-TBQ-based OPV ( $\sim 35\%$ ) at the wavelength of 420 nm.

**TABLE 4** PL Decay Parameters of the Neat Polymers and Blend Films

Sample	A (%)	$\tau$ (ps)	A <sub>e</sub> (%)	$\tau_e$ (ps)
PBDT-TBQ	83	0.68	17	9.23
PBDT-TBQ:PC <sub>71</sub> BM	83	0.62	17	7.64
PBDT-TPQ	78	0.81	22	8.67
PBDT-TPQ:PC <sub>71</sub> BM	82	0.67	18	11.74

## CONCLUSIONS

In conclusion, we have designed and synthesized two new D- $\pi$ -A copolymers, PBDT-TBQ and PBDT-TPQ, based on a BDT donor moiety together with a BQ or a PQ acceptor unit bridged by the thiophene between the donor and acceptor units, for studies on the relationship of the molecular structure and photovoltaic performance. The results showed that by the incorporation of strong electron-withdrawing PQ unit, PBDT-TPQ copolymer not only offered excellent solubility and thermal stability but also exhibited many desirable advantages such as deeper HOMO and LUMO energy levels, semicrystallinity, and higher hole mobility. In comparison with PBDT-TBQ, PBDT-TPQ promoted the formation of well-organized domains in the polymer blend, in agreement with the red-shifted absorption spectra, enhanced charge mobility, photocurrent, and FF of the corresponding devices. The experimental data showed that the exciton dissociation efficiency of PBDT-TPQ:PC<sub>71</sub>BM blend was better than that in the PBDT-TBQ:PC<sub>71</sub>BM blend, which can be used to explain that the IPCE spectra of the PBDT-TPQ-based solar cell were higher than that of the PBDT-TBQ-based solar cell. Solar efficiencies of the best performing PBDT-TBQ- and PBDT-TPQ-based devices were 2.45% and 4.40% in an inverted device architecture, suggesting that PQ moiety could be a novel promising building block for organic semiconducting materials.

## ACKNOWLEDGMENTS

This work was financially supported by the Ministry of Science and Technology of Taiwan. The device fabrication was carried out in the Advanced Laboratory of Accommodation and Research for Organic Photovoltaics, Ministry of Science and Technology of Taiwan. The authors thank Ting-Yang Kuo and Chun-Hsien Chen, National Taiwan University, for their support with the atomic force microscopy.

## REFERENCES AND NOTES

- 1 S. R. Forrest, *Nature* **2004**, *428*, 911.
- 2 W. Chen, M. P. Nikiforov, S. B. Darling, *Energy Environ. Sci.* **2012**, *5*, 8045–8074.
- 3 L. Dou, J. You, Z. Hong, Z. Xu, G. Li, R. A. Street, Y. Yang, *Adv. Mater.* **2013**, *25*, 6642–6671.
- 4 J. H. Kim, H. S. Kim, J. B. Park, I. N. Kang, D. H. Hwang, *J. Polym. Sci. Part A: Polym. Chem.* **2014**, *52*, 3608–3616.

- 5 J. H. Kim, J. B. Park, F. Xu, D. Kim, J. Kwak, A. C. Grimsdale, D. H. Hwan, *Energy Environ. Sci.* **2014**, *7*, 4118–4131.
- 6 Y. Sun, C. Zhang, B. Dai, B. Lin, H. Yang, X. Zhang, L. Guo, Y. Liu, *J. Polym. Sci. Part A: Polym. Chem.* **2015**, *53*, 1915–1926.
- 7 H. Zhou, L. Yang, W. You, *Macromolecules* **2012**, *45*, 607–632.
- 8 H. Kim, H. Lee, D. Seo, Y. Jeong, K. Cho, J. Lee, Y. Lee, *Chem. Mater.* **2015**, *27*, 3102–3107.
- 9 M. Zhang, X. Guo, W. Ma, S. Zhang, L. Huo, H. Ade, J. Hou, *Adv. Mater.* **2014**, *26*, 2089–2095.
- 10 S. Wen, X. Bao, W. Shen, C. Gu, Z. Du, L. Han, D. Zhu, R. Yang, *J. Polym. Sci. Part A: Polym. Chem.* **2014**, *52*, 208–215.
- 11 A. C. Stuart, J. R. Tumbleston, H. X. Zhou, W. T. Li, S. B. Liu, H. Ade, W. You, *J. Am. Chem. Soc.* **2013**, *135*, 1806–1815.
- 12 H. C. Chen, Y. H. Chen, C. H. Liu, Y. H. Hsu, Y. C. Chien, W. T. Chuang, C. Y. Cheng, C. L. Liu, S. W. Chou, S. H. Tung, P. T. Chou, *J. Polym. Sci. Part A: Polym. Chem.* **2013**, *4*, 3411–3418.
- 13 Y. Fu, H. Cha, S. Song, G. Y. Lee, C. E. Park, T. Park, *J. Polym. Sci. Part A: Polym. Chem.* **2013**, *51*, 372–382.
- 14 K. W. Song, T. H. Lee, E. J. Ko, K. H. Back, D. K. Moon, *J. Polym. Sci. Part A: Polym. Chem.* **2014**, *52*, 1028–1036.
- 15 H. C. Chen, Y. H. Chen, C. C. Liu, Y. C. Chien, S. W. Chou, P. T. Chou, *Chem. Mater.* **2012**, *24*, 4766–4772.
- 16 M. Zhang, Y. Gu, X. Guo, F. Liu, S. Zhang, L. Huo, T. P. Russell, J. Hou, *Adv. Mater.* **2013**, *25*, 4944–4949.
- 17 I. Osaka, T. Kakara, N. Takemura, T. Koganezawa, K. Takimiya, *J. Am. Chem. Soc.* **2013**, *135*, 8834–8837.
- 18 M. Zhang, X. Guo, S. Zhang, J. Hou, *Adv. Mater.* **2014**, *26*, 1118–1123.
- 19 C. Z. Li, C. Y. Chang, Y. Zang, H. X. Ju, C. C. Chueh, P. W. Liang, N. Cho, D. S. Ginger, A. K. Y. Jen, *Adv. Mater.* **2014**, *26*, 6262–6267.
- 20 Z. He, C. Zhong, X. Huang, W. Y. Wong, H. Wu, L. Chen, S. Su, Y. Cao, *Adv. Mater.* **2011**, *23*, 4636–4643.
- 21 X. Li, W. C. H. Choy, L. Huo, F. Xie, W. E. I. Sha, B. Ding, X. Guo, Y. Li, J. Hou, J. You, Y. Yang, *Adv. Mater.* **2012**, *24*, 3046–3052.
- 22 Z. G. Zhang, B. Qi, Z. Jin, D. Chi, Z. Qi, Y. Li, J. Wang, *Energy Environ. Sci.* **2014**, *7*, 1966–1973.
- 23 Z. Zhang, F. Lin, H. C. Chen, H. C. Wu, C. L. Chung, C. Lu, S. H. Liu, S. H. Tung, W. C. Chen, K. T. Wong, P. T. Chou, *Energy Environ. Sci.* **2015**, *8*, 552–557.
- 24 S. Xiao, L. Chen, L. Tan, L. Huang, F. Wu, Y. Chen, *J. Phys. Chem. C* **2015**, *119*, 1943–1952.
- 25 S. Liu, K. Zhang, J. Lu, J. Zhang, H. L. Yip, F. Huang, Y. Cao, *J. Am. Chem. Soc.* **2013**, *135*, 15326–15329.
- 26 Y. L. Li, Y. S. Cheng, P. N. Yeh, S. H. Liao, S. A. Chen, *Adv. Funct. Mater.* **2014**, *24*, 6811–6817.
- 27 C. C. Chueh, C. Z. Li, A. K. Y. Jen, *Energy Environ. Sci.* **2015**, *8*, 1160–1189.
- 28 H. C. Chen, S. W. Chou, W. H. Tseng, I. -W. P. Chen, C. C. Liu, C. Liu, C. L. Liu, C. Chen, C. I. Wu, P. T. Chou, *Adv. Funct. Mater.* **2012**, *22*, 3975–3984.
- 29 W. Sun, H. Peng, Y. Li, W. Yan, Z. Liu, Z. Bian, C. Huang, *J. Phys. Chem. C* **2014**, *118*, 16806–16812.
- 30 S. W. Chou, H. C. Chen, Z. Zhang, W. H. Tseng, C. I. Wu, Y. Y. Yang, C. Y. Lin, P. T. Chou, *Chem. Mater.* **2014**, *26*, 7029–7038.
- 31 S. Liu, P. You, J. Li, J. Li, C. S. Lee, B. S. Ong, C. Surya, F. Yan, *Energy Environ. Sci.* **2015**, *8*, 1463–1470.
- 32 C. Duan, K. Zhang, C. Zhong, F. Huang, Y. Cao, *Chem. Soc. Rev.* **2013**, *42*, 9071–9104.
- 33 J. M. Jiang, P. A. Yang, H. C. Chen, K. H. Wei, *Chem. Commun.* **2011**, *47*, 8877–8879.
- 34 J. M. Jiang, P. A. Yang, C. M. Yu, H. K. Lin, K. C. Huang, K. H. Wei, *J. Polym. Sci. Part A: Polym. Chem.* **2012**, *50*, 3960–3969.
- 35 J. M. Jiang, H. K. Lin, Y. C. Lin, H. C. Chen, S. C. Lan, C. K. Chang, K. H. Wei, *Macromolecules* **2014**, *47*, 70–78.
- 36 V. D. Mihailetchi, L. J. A. Koster, P. W. M. Blom, C. Melzer, B. de Boer, J. K. J. van Duren, R. A. J. Janssen, *Adv. Funct. Mater.* **2005**, *15*, 795–801.
- 37 V. D. Mihailetchi, H. Xie, B. de Boer, L. J. A. Koster, P. W. M. Blom, *Adv. Funct. Mater.* **2006**, *16*, 699–708.
- 38 N. Zhou, K. Prabakaran, B. Lee, S. H. Chang, B. Harutyunyan, P. Guo, M. R. Bulter, A. Timalisina, M. J. Bedzyk, M. A. Ratner, S. Vegiraju, S. Yau, C. G. Wu, R. P. H. Chang, *J. Am. Chem. Soc.* **2015**, *137*, 4414–4423.
- 39 R. C. Coffin, J. Peet, J. Rogers, G. C. Bazan, *Nat. Chem.* **2009**, *1*, 657–661.
- 40 B. Schmidt-Hansberg, M. Sanyal, M. F. G. Klein, M. Pfaff, N. Schnabel, S. Jaiser, A. Vorobiev, E. Muller, A. Colsmann, P. Scharfer, D. Gerthsen, U. Lemmer, E. Barrera, W. Schabel, *ACS Nano* **2011**, *5*, 8579–8590.
- 41 J. Rivnay, S. C. B. Mannsfeld, C. E. Miller, A. Salleo, M. F. Toney, *Chem. Rev.* **2012**, *112*, 5488–5519.
- 42 K. H. Hendriks, G. H. L. Heintges, V. S. Gevaerts, M. Wienk, R. A. J. Janssen, *Angew. Chem. Int. Ed. Engl.* **2013**, *52*, 8341–8344.
- 43 W. Li, L. Yang, J. R. Tumbleston, L. Yan, H. Ade, W. You, *Adv. Mater.* **2014**, *26*, 4456–4462.
- 44 S. H. Chang, C. H. Chiang, H. M. Cheng, C. Y. Tai, C. G. Wu, *Opt. Lett.* **2013**, *38*, 5342–5345.
- 45 S. H. Chang, C. H. Chiang, Z. L. Tseng, K. Y. Chiu, C. Y. Tai, C. G. Wu, *J. Phys. D: Appl. Phys.* **2015**, *48*, 195104.